Applied Physics Letters ACCEPTED MANUSCRIPT
This is the author's peer reviewed, accepted manuscript. However, the online version of record will be different from this version once it has been copyedited and typeset.
PLEASE CITE THIS ARTICLE AS DOI: 10.1063/5.0032969
AIP Publishing

Real-time imaging and tracking of microrobots in tissues using ultrasound phase analysis

S. Pane,[1,2,a)] V. Iacovacci,[1,2] E. Sinibaldi [3] and A. Menciassi[1,2]

[1] *The BioRobotics Institute, Scuola Superiore Sant'Anna, Pisa, Italy, 56025*

[2] *Department of Excellence in Robotics & AI, Scuola Superiore Sant'Anna, Pisa, Italy, 56127*

[3] *Center for Micro-BioRobotics, Istituto Italiano di Tecnologia, Pontedera, Italy, 56025*

[a)] Corresponding author (stefano.pane@santannapisa.it)

ABSTRACT

Ultrasound B-mode imaging has been employed to monitor single agents and collective swarms of microrobots in-vitro and ex-vivo, in controlled experimental conditions. However, low contrast and spatial resolution still limit the effective employment of such method in a medical microrobotic scenario. Doppler-based ultrasound appears as a promising tool for tracking microrobots in echogenic and dynamic environments as biological tissues. In this letter we demonstrate that microrobot displacements can be used as a special signature for their visualization within echogenic media, where B-mode fails. To this aim, we induced vibrations of a magnetic soft microrobot through alternated magnetic fields and used ultrasound phase analysis to derive microrobot features such as size and position over time. By exploiting vibrations, we were able to perform imaging and tracking of a low contrast microrobot both in tissue-mimicking phantom and in chicken breast. Axial resolution was 38µm, that is four times smaller than the B-mode resolution with the employed equipment. We also performed real-time tracking of the microrobot's positions along linear trajectories with a linear velocity up to 1mm/s. Overall, the reported results pave the way to the application of the proposed approach for the robust monitoring of medical microrobots in tissue.

Over the past decade, medical microrobotics has been taking a major leap forward to bridge the gap between available technology and science fiction[1–3]. When targeting non-invasive biomedical applications based on microrobots (MR), therapy success highly depends on the integration of therapeutic functionalities and controlled navigation[4]. Imaging strategies functional to real-time MR tracking in tissue are crucial, but they remain an open issue [5]. Among traditional medical imaging techniques, ultrasound (US) combines good spatial resolution (100-500µm) and deep tissue real-time imaging (up to 25 cm far from the probe) with no adverse health effects and low equipment cost [6]. In the past few years, Brightness(B)-mode US imaging has been employed to monitor navigation and cargo delivery performed both by single agents and collective MR swarms [7–14]. However, B-mode relies on objects echogenicity, i.e., the ability to scatter US waves back to the source. Image contrast depends on the intensity of the backscattered waves and on its difference with respect to the signal produced by the surrounding medium. For this reason, most of state of the art works report about MR visualization within still, homogeneous and scarcely echogenic media (e.g. glycerol oil, vitreous humor), used to improve imaging contrast [15,16]. On the other hand, as a result of inhomogeneity and

Applied Physics Letters ACCEPTED MANUSCRIPT

This is the author's peer reviewed, accepted manuscript. However, the online version of record will be different from this version once it has been copyedited and typeset.

PLEASE CITE THIS ARTICLE AS DOI: 10.1063/5.0032969

AIP Publishing

discontinuities in acoustic impedance, biological tissues are highly echogenic and produce high contrast imaging artifacts. Due to the lack of contrast resolution in B-mode, i.e. the ability to distinguish between different intensity levels in the image, imaging artifacts hamper the visualization of MR, calling for medical/technical specialists to analyze the images thus limiting the automatization of the process. Although a possible solution for contrast enhancement stands in the MR functionalization with specific contrast agents such as microbubbles, these suffer from short half-life [17,18]. In addition to low contrast resolution, B-mode spatial resolution is also unsuitable for detecting MR features which are smaller than the transmitted US wavelength λ (100-500μm for commercial equipment, working in a range of 3-15MHz), due to waves diffraction phenomena. US Doppler-based methods can help overcoming these limitations by allowing to detect displacements smaller than λ [19–21]. These techniques analyze the acoustic phase signal extracted from the radiofrequency (RF) US data, which contain motion information not depending on echogenicity. Although promising, these techniques have only been implemented offline in elastography applications so far and they have never been employed for real-time imaging and tracking of MR.

In this letter we propose an approach which exploits MR displacements as a special signature for their detection within highly echogenic and dynamic environments, as biological tissues are. To verify this approach, we induced the vibration of a magneto-responsive soft MR through alternating magnetic fields. Vibrations were detected through US phase analysis and processed to properly visualize the MR in high contrast background and to derive features such as size and position over time.

The experimental validation platform comprised an agar-based tissue-mimicking phantom embedding the magnetic MR, an alternating magnetic fields source and a US vibration detection unit (Figure 1A). The magnetic soft MR consisted of agarose gel doped with paramagnetic nanoparticles. Vibrations of the MR were generated by alternating magnetic fields, through the rotation of a cylindrical permanent magnet (6cm in diameter, 7cm in height, NdFeB, diametral magnetization, grade N35) attached to the end-effector of a robotic arm (Melfa-RV3S, Mitsubishi). A dedicated physical model allowed to induce vibrations with controlled amplitude and frequency, by adjusting magnetic field parameters (see supplementary material). The phantom containing the vibrating MR was imaged with a standard 10MHz US linear probe (L15-7H40, Telemed) and dedicated signal processing algorithms enabled to detect MR vibrations. To ensure good acoustic coupling, the phantom was submerged in a water tank provided with a pyramidal acoustic absorber.

For detecting vibrations through US, we exploited the effect of modulation of the acoustic signal phase induced by axial displacements [22]. In particular, when transmitting a sinusoidal pulse, the analytic signal $E^*(t)$ containing the echoes relative to a single US beam (i.e., a scan line) is expressed as follows:

$$E^*(t) = A(t) \cdot \mathrm{e}^{j\varphi(t)} \tag{1}$$

where $A(t)$ is the instantaneous amplitude of the signal, also known as the envelope, while $\varphi(t)$ is the instantaneous phase. The envelope carries information about the intensity of the pressure wave that is locally backscattered by each object along the wave path. B-mode converts $A(t)$ into brightness levels to create a contrast image. However, this implies that if the MR is close to a more echogenic object (e.g. the boundary of a vessel lumen) it cannot be detected by looking at the envelope signal [23]. Furthermore, displacements smaller than λ are not detectable in B-mode due to the loss of information resulting from the envelope operation (Figure 1B).

Applied Physics Letters ACCEPTED MANUSCRIPT

This is the author's peer reviewed, accepted manuscript. However, the online version of record will be different from this version once it has been copyedited and typeset.

PLEASE CITE THIS ARTICLE AS DOI: 10.1063/5.0032969

AIP Publishing

Figure 1. Working principle and experiments overview. (A) Experimental setup for imaging and tracking of vibrating microrobots and its constitutive components, namely the vibration detection unit *a*, the phantom with the embedded microrobot *b*, and the alternating magnetic fields source *c*. The controlled rotation of a magnet induces microrobot vibrations while a linear stage generates the relative motion of the microrobot in the imaging plane. (B) Phase modulation of the acoustic signal induced by axial displacements and real measurements of echoes reflected by objects in positions 1,2 and 3 along the acoustic axis *y*. The proximity of a high contrast object, e.g., the lumen boundary in position 3, hampers the visualization of a lower contrast object, e.g., MR vibrating between positions 1 and 2. Displacements smaller than λ are not detectable in B-mode due to the loss of information resulting from the envelope operation.

Such small displacements can be detected by analyzing the phase $\varphi(t)$ of backscattered echoes, instead of $A(t)$ [22]. If an object moves from position 1 to position 2 along the direction of wave propagation (i.e., the acoustic axis), the echoes backscattered from the two positions present an instantaneous phase difference $\partial\varphi$ which is linearly proportional to the object displacement u (Fig. 1B):

$$\partial\varphi = \varphi_2(t) - \varphi_1(t) = u\frac{4\pi}{\lambda} \qquad (2)$$

This can be extended to displacements in any direction, by considering their projection along the acoustic axis (y).

By exploiting this principle, MR vibrations intended as harmonic displacements can be considered as signature for MR detection. The processing steps implemented for MR detection are illustrated in Figure 2. Displacements are reflected on the phase variations in RF data. The RF data associated to n consecutive frames are typically stored in a 3D matrix, called cineloop. The first dimension of the cineloop is the index of the scan line (i.e., the single piezoelectric element of the probe - x), whereas the second is the so-called fast-time (y) and represents the direction of wave propagation. The third is the so-called slow-time (n), and represents the index of acquired frames in time. The analytic acoustic signal E^* is obtained from the RF data cineloop through the Hilbert transform. Defining a generic coordinate (x, y) in the cineloop as a sub-pixel, the value of E^* at frame n can be expressed as:

$$E^*(x, y, n) = A(x, y, n) \cdot \mathrm{e}^{j\varphi(x,y,n)} \qquad (3)$$

Objects displacements within the sub-pixel (x, y) along an ensemble of consecutive frames are modulated on φ (eq. 2), thus on the argument of E^* unwrapped on the slow-time n.

$$\varphi(x, y, n) = \arg(E^*(x, y, n), n) \qquad (4)$$

By evaluating the Fast Fourier Transform (FFT) of φ along n, the frequency spectra $S(x, y, f)$ are obtained, containing information on displacements in the frequency domain.

Applied Physics Letters ACCEPTED MANUSCRIPT

This is the author's peer reviewed, accepted manuscript. However, the online version of record will be different from this version once it has been copyedited and typeset.

PLEASE CITE THIS ARTICLE AS DOI: 10.1063/5.0032969

AIP Publishing

$$S(x, y, f) = \mathrm{FFT}(\varphi(x, y, n), n) \tag{5}$$

MR vibrations are induced through a sinusoidal magnetic force signal, produced by the rotation of a magnet:

$$F_{mag}(t) = M\mathrm{e}^{j(2\pi f_{mag} t + \psi_{mag})} \tag{6}$$

where f_{mag} is the magnet rotation frequency and ψ_{mag} the phase. MR vibration frequency, identified by the peak in the modulus of the frequency spectrum $S(x, y, f)$, is approximately f_{mag} if both viscoelasticity and other non-linearities are negligible. For isolating vibrations of interest, both modulus and phase of $S(x, y, f)$ are band-pass filtered at f_{mag}, employing the Goertzel algorithm[24] for its time-efficiency.

$$F(x, y) = \mathrm{bandpass}(S(x, y, f), f_{mag}) \tag{7}$$

The modulus of $F(x, y)$ contains the amplitude of vibrations at f_{mag} for each sub-pixel. Applying the inverse Fourier transform to $F(x, y)$ and demodulating according to equation (2), a 2D Motion Image (MI) is obtained.

$$MI(x, y) = \mathrm{IFFT}\big(F(x, y)\big) * \frac{c}{4\pi f} \tag{8}$$

In a dynamic environment as the human body, there is a manifold of background motions (either real or noise-generated) containing a component at f_{mag}, which is included in $MI(x, y)$. The entity of such components could be larger than the entity of the MR vibrations, making the latter poorly visible. However, the MR can be distinguished from other vibrating regions by selecting the sub-pixels signals that are in-phase with the excitation field. In particular, to exclude out-of-phase vibrations a phase filter is implemented. First, the phase of $F(x, y)$, referred to as the Phase Distribution of Vibrating Sub-pixels (PDVS), is inspected. In-phase sub-pixels are concentrated around ψ_{mag}in a distribution that is referred to as the Phase Distribution of Synchronous Sub-pixels (PDSS). The value of ψ_{mag} is identified by the PDSS peak and a phase window is defined by its half width at half maximum w. Finally, a filter is applied to the Motion Image to select the sub-pixels included in the identified phase window: if the phase of vibration is outside the window, the sub-pixel intensity is set to zero. The image obtained after this step is referred to as Filtered Motion Image (FMI).

Figure 2. Processing algorithm workflow and representative results. The acoustic analytic signal is extracted from the RF data cineloop through the Hilbert transform. The amplitude of this signal is used for B-mode imaging while the acoustic phase is unwrapped along the slow-time dimension n. The frequency spectra of the acoustic phase are obtained through the FFT. Both modulus and phase of the spectra are band-pass filtered at f_{mag} in order to detect magnetically induced vibrations. The filtered modulus is used to build a motion image while the filtered phase (PDVS) is used to identify magnetic signal phase ψ_{mag} and build a windowing phase filter. The phase filter applied to the motion image outputs a filtered motion image, displaying only the in-phase vibrations (as in the Filtered Motion Image box). The microrobot, not visible in B-mode, is clearly visible in the filtered motion image, which is used for localization and for tracking its features, by merging with the B-mode image. Scale bar is 1 mm. Illustrative outcomes of the process along the pipeline are displayed by the brighter arrows in the flowchart.

Applied Physics Letters ACCEPTED MANUSCRIPT

This is the author's peer reviewed, accepted manuscript. However, the online version of record will be different from this version once it has been copyedited and typeset.

PLEASE CITE THIS ARTICLE AS DOI: 10.1063/5.0032969

AIP Publishing

We employed the FMI to detect a vibrating MR in a highly echogenic medium and in presence of boundaries. To test the robustness of this method, we included the magnetic MR in a multilayered phantom in which the interface between two layers can simulate the boundary of a lumen (Figure 3A). The MR was not clearly visible in B-mode as its contrast was comparable to that of the random speckle pattern of the image. On the other hand, boundaries (white lines) showed the highest contrast. Remarkably, when the MR was put into vibration through the external magnetic field, it was clearly visualized and localized in the FMI. The MR centroid was identified by the sub-pixel exhibiting the maximum vibration amplitude (see the physical model in supplementary material). The axial resolution of a sub-pixel is improved with respect to that of a B-mode pixel (Figure 3B). In fact, if the speed of sound in the phantom is about 1500m/s and we use a probe with center frequency 10MHz, the B-mode pixel has an axial dimension of 150µm. On the other hand, with the same speed of sound, if the acoustic signal is digitalized at a 40MHz sampling rate, the sub-pixel axial size is 38µm (four times smaller than B-mode). In this sense, the proposed approach offers an improved axial resolution, which is dependent on the sampling rate of the acquisition system but independent on λ, thus not subject to the typical resolution/depth trade-off characterizing B-mode imaging[25]. When no magnetic excitation is present (static condition, Figure 3C), the frequency spectrum of the displacement signal of the sub-pixel corresponding to the MR centroid includes only white noise components, arising from various phenomena (e.g., diffuse scattering, diffraction, electromagnetic noise, digitalization). The average level of white noise in the spectrum varies with imaging hardware and experimental conditions. In order to be detectable with this technique, the amplitude of the vibration signal must be larger than the noise threshold. Considering the experimental setup employed in this study, noise is comparable to the signal produced by 1µm wide vibrations in phantom experiments (red dotted line in Figure 3C). Therefore, vibrational amplitude should be tuned to overcome the noise threshold by properly adjusting magnetic field parameters and MR mechanical and magnetic properties. For a detailed description of the physical model used for inducing vibrations and for a quantitative evaluation of the effects of vibration amplitude on the imaging capabilities, the reader may refer to the supplementary material (Figure 3S). The PDVS exhibits a normal distribution in static conditions, resulting from noise. When the magnetic field is turned on, the spectrum of the displacement signal includes the contribution of magnetically induced vibrations (black-dashed box in Fig. 3C) and the PDVS exhibits two peaks: a larger one associated to noise and a shorter one, the PDSS, associated to the in-phase motions of all sub-pixels containing the MR body (black-dashed curve in Fig. 3C).

Figure 3. Imaging of a vibrating microrobot in phantom and ex-vivo chicken breast. (A) schematic representation of the multilayered phantom embedding the microrobot and comparison between B-mode and filtered motion image (FMI). The white box represents the region containing the MR. (B) Comparison of MR visualization in B-mode (top) and FMI (bottom). The MR can be easily distinguished from the boundary through the FMI. The improved axial resolution of FMI allows to visualize the distribution of vibration amplitudes within the MR body. (C) Comparison of US signals acquired in static conditions (no magnetic excitation) and during vibrations. (D) Comparison between standard B-mode and FMI (superimposed on B-mode) of chicken breast tissue embedding the MR. The MR can be easily distinguished from imaging artifacts through the FMI. The correct imaging plane containing the MR was identified through the use of polystyrene markers. The white box represents the region containing the MR.

Image processing parameters, such as the modulus of the peak frequency component and the PDSS peak and width, were identified here by automatic peak detection algorithms (e.g., by evaluation of local maxima). This strategy allows to identify vibrational frequency and phase also when they are not known a priori. To

Applied Physics Letters ACCEPTED MANUSCRIPT

This is the author's peer reviewed, accepted manuscript. However, the online version of record will be different from this version once it has been copyedited and typeset.
PLEASE CITE THIS ARTICLE AS DOI: 10.1063/5.0032969

AIP Publishing

validate the approach in biological tissues, we performed ex-vivo experiments in chicken breast. The MR was placed between two layers of tissue, together with polystyrene spheres used as markers for helping in imaging plane (*xy*) identification (Figure 3D). As a result of tissue inhomogeneity, the random speckle pattern in the B-mode image featured high contrast, resulting in highly echogenic imaging artifacts that prevented MR visualization. On the contrary, by exploiting magnetically induced vibrations, the MR was visualized and localized in the FMI. Overall, the results of ex-vivo experiments were in full agreement with phantom experiments, validating the feasibility of the proposed technique for detecting vibrating MRs in biological tissues.

Lastly, the approach was validated through tracking experiments. Linear trajectories of the MR within the imaging plane were simulated by moving the US probe with respect to the phantom along the x direction, with reference to Figure 1A. The localization algorithm was run continuously to provide FMIs in real-time. At the first iteration, the tracking algorithm performs blind localization to identify the MR position without any a priori knowledge. Localization is then continued within a reduced search window (RSW), in the neighborhood of the last registered MR position, thus reducing the computational burden and the effects of white noise in the PDVS. The PDVS evaluated in the RSW, in fact, incorporated less noise contributions featuring a more prominent PDSS with respect to that obtained during blind localization, thus favoring a more robust automatic peak detection (Figure 4A). The RSW dimension were adapted to the MR size and velocity, both estimated from the analysis of the previous images. With the considered experimental conditions (diameter of 1.5mm and vibration frequency of 3Hz) dynamic tracking of the MR centroid over a 10s acquisition time, with a frame rate of 1.5fps, was performed for different linear velocities, spanning from zero to 1mm/s. Tracked centroid trajectories for three considered velocities (0.2mm/s, 0.5mm/s, 1mm/s), reported in Figure 4B, show good agreement with linear fits (R^2 of 0.9, 0.86, 0.81, respectively), thus supporting the potential employment of the proposed approach for real-time tracking of MR. The analysis of FMIs acquired during linear trajectories demonstrated the visualization of the MR also in dynamic conditions (Figure 4C). The MR vibration frequency defines the observation time required for one localization, thus influencing both the tracking frame rate and the maximum trackable linear velocity. In particular, faster tracking and higher trackable MR velocities are enabled by higher vibration frequencies. For a more detailed discussion on the influence of the vibration frequency on the tracking performances, the reader may refer to the supplementary material (Figure 4S).

In conclusion, in this work we exploited magnetically induced vibrations to obtain a signature allowing for MR imaging and tracking in echogenic and dynamic tissues, where standard B-mode fails. We validated MR detection both in phantom and in chicken breast tissue. We also demonstrated tracking of the MR along linear trajectories with speed up to 1mm/s. Considering the effects of background noise on the acoustic phase signal, the vibration amplitude is a key parameter for this imaging technique and must be large enough to provide an adequate signal-to-noise ratio. On the other hand, higher vibration frequencies enable faster tracking and higher maximum trackable MR velocity. The limits on trackable velocity can be overcome by moving the US probe to adaptively follow MR trajectories, as in visual servoing systems. In this way, artifacts due to the translation of centroid during the localization observation time would be minimized (see last section of supplementary material).

Figure 4. Dynamic tracking experiments results. (A) The employment of a reduced search window minimizes noise effects, resulting in a more prominent PDSS. (B) Tracked trajectories of the MR centroid (orange dot) for different linear velocities (0.2mm/s, 0.5mm/s, 1mm/s) show good agreements with linear fits (red lines). The coefficients of determination are 0.9, 0.86, 0.81, respectively. The MR is represented by the red circular body. (C) Overlapped FMIs displaying the MR along a linear trajectory validate correct visualization during dynamic tracking.

Applied Physics Letters ACCEPTED MANUSCRIPT

This is the author's peer reviewed, accepted manuscript. However, the online version of record will be different from this version once it has been copyedited and typeset.

PLEASE CITE THIS ARTICLE AS DOI: 10.1063/5.0032969

AIP Publishing

The proposed approach provides enhanced axial resolution compared to B-mode resolution (four times better for the adopted conditions): such an improvement is independent on the US wavelength thus allowing, in principle, for high resolution imaging at higher penetration depths, provided that the effects of wave attenuation are properly compensated. Overall, the reported results pave the way to the application of the proposed approach for monitoring medical microrobotics tasks in biological tissue, based on characterized vibration patterns of either the entire structure or a portion of the MR.[16,26–30] Further developments of this work will aim to extend the technique to the 3D case (e.g., through matrix phased arrays), by considering that the longer data acquisition times pose additional challenges to the achievement of real-time imaging and tracking. Future studies should also focus on *in vivo* applicability, where physiological motions (e.g., breathing, heartbeat) pose additional challenges to motion detection. To this purpose, deeper investigations should aim at extending this technique to non-harmonic signals, thus enabling the detection of a wider class of motion patterns.

SUPPLEMENTARY MATERIAL

The reader may refer to the supplementary material for more details on *i*) the experimental setup design *ii*) the phantom and MR fabrication *iii*) a complete description and validation of the physical model developed for determining the magnetically induced vibrations *iv*) a characterization of how vibration parameters (e.g., amplitude and frequency) affects the imaging capabilities of the proposed approach.

DATA AVAILABILITY

The data that support the findings of this study are available from the corresponding author upon reasonable request.

Applied Physics Letters ACCEPTED MANUSCRIPT

This is the author's peer reviewed, accepted manuscript. However, the online version of record will be different from this version once it has been copyedited and typeset.

PLEASE CITE THIS ARTICLE AS DOI: 10.1063/5.0032969

AIP Publishing

Bibliography

[1] B.J. Nelson, I.K. Kaliakatsos, and J.J. Abbott, Annu. Rev. Biomed. Eng. **12**, 55 (2010).

[2] J. Wang, R. Dong, H. Wu, Y. Cai, and B. Ren, Nano-Micro Lett. **12**, (2020).

[3] X.Z. Chen, B. Jang, D. Ahmed, C. Hu, C. De Marco, M. Hoop, F. Mushtaq, B.J. Nelson, and S. Pané, Adv. Mater. **30**, 1 (2018).

[4] H. Ceylan, I.C. Yasa, U. Kilic, W. Hu, and M. Sitti, Prog. Biomed. Eng. **1**, 12002 (2019).

[5] M. Medina-s, O.G. Schmidt, M. Medina-Sánchez, and O.G. Schmidt, Nature **545**, 406 (2017).

[6] A. Aziz, S. Pane, V. Iacovacci, N. Koukourakis, J. Czarske, A. Menciassi, M. Medina-Sánchez, and O.G. Schmidt, ACS Nano (2020).

[7] D. Li, M. Jeong, E. Oren, T. Yu, and T. Qiu, Robotics **8**, 87 (2019).

[8] E.E. Niedert, C. Bi, G. Adam, E. Lambert, L. Solorio, C. Goergen, and D.J. Cappelleri, BioRxiv (2020).

[9] Z. Ren, T. Wang, W. Hu, and M. Sitti, in *Robot. Sci. Syst.* (2019).

[10] F.A. Blyakhman, L.Y. Iskakova, M.T. Lopez-Lopez, and A.Y. Zubarev, J. Magn. Magn. Mater. **478**, 211 (2019).

[11] Q. Wang, J. Yu, K. Yuan, L. Yang, D. Jin, and L. Zhang, Appl. Mater. Today **18**, 100489 (2020).

[12] V. Magdanz, I.S.M. Khalil, J. Simmchen, G.P. Furtado, S. Mohanty, J. Gebauer, H. Xu, A. Klingner, A. Aziz, M. Medina-Sánchez, O.G. Schmidt, and S. Misra, Sci. Adv. **6**, eaba5855 (2020).

[13] F. Ongaro, D. Niehoff, S. Mohanty, and S. Misra, Micromachines **10**, 504 (2019).

[14] Q. Wang, L. Yang, J. Yu, P.W.Y. Chiu, Y.-P. Zheng, and L. Zhang, IEEE Trans. Biomed. Eng. (2020).

[15] I.S.M. Khalil, P. Ferreira, R. Eleutério, C.L. de Korte, and S. Misra, in *2014 IEEE Int. Conf. Robot. Autom.* (IEEE, 2014), pp. 3807–3812.

[16] J. Yu, D. Jin, K.F. Chan, Q. Wang, K. Yuan, and L. Zhang, Nat. Commun. **10**, 5631 (2019).

[17] R. Bourdeau, A. Lee-Gosselin, A. Lakshmanan, S. Kumar, A. Farhadi, and M. Shapiro, Nat. Publ. Gr. **553**, 86 (2018).

[18] T. Segers, E. Gaud, G. Casqueiro, A. Lassus, M. Versluis, and P. Frinking, Appl. Phys. Lett. **116**, 173701 (2020).

[19] A.G. Pope, G. Wu, F.Y. McWhorter, E.P. Merricks, T.C. Nichols, T.J. Czernuszewicz, C.M. Gallippi, and A.L. Oldenburg, Phys. Med. Biol. **58**, 7277 (2013).

[20] M. Evertsson, M. Cinthio, S. Fredriksson, F. Olsson, H. Persson, and T. Jansson, IEEE Trans. Ultrason. Ferroelectr. Freq. Control **60**, 481 (2013).

[21] M. Fink, S. Lyer, C. Alexiou, S.J. Rupitsch, and H. Ermert, Curr. Dir. Biomed. Eng. **5**, 417 (2019).

[22] M.W. Urban, S. Chen, and J.F. Greenleaf, IEEE Trans. Ultrason. Ferroelectr. Freq. Control **55**, 1956 (2008).

[23] H. Azhari, *Basics of Biomedical Ultrasound for Engineers* (John Wiley and Sons, 2010).

[24] P. Sysel and P. Rajmic, EURASIP J. Adv. Signal Process. **2012**, 56 (2012).

[25] H. Azhari, *Basics of Biomedical Ultrasound for Engineers* (John Wiley & Sons, 2010).

[26] J. Yu, B. Wang, X. Du, Q. Wang, and L. Zhang, Nat. Commun. **9**, 1 (2018).

[27] W. Hu, G.Z. Lum, M. Mastrangeli, and M. Sitti, Nature **554**, 81 (2018).

[28] I.S.M. Khalil, H.C. Dijkslag, L. Abelmann, and S. Misra, Appl. Phys. Lett. **104**, (2014).

[29] K. Vollmers, D.R. Frutiger, B.E. Kratochvil, and B.J. Nelson, Appl. Phys. Lett. **92**, 144103 (2008).

[30] F. Becker, V. Lysenko, V.T. Minchenya, O. Kunze, and K. Zimmermann, in *Microactuators and Micromechanisms* (Springer, 2017), pp. 91–102.

Applied Physics Letters ACCEPTED MANUSCRIPT

This is the author's peer reviewed, accepted manuscript. However, the online version of record will be different from this version once it has been copyedited and typeset.

PLEASE CITE THIS ARTICLE AS DOI: 10.1063/5.0032969

AIP Publishing

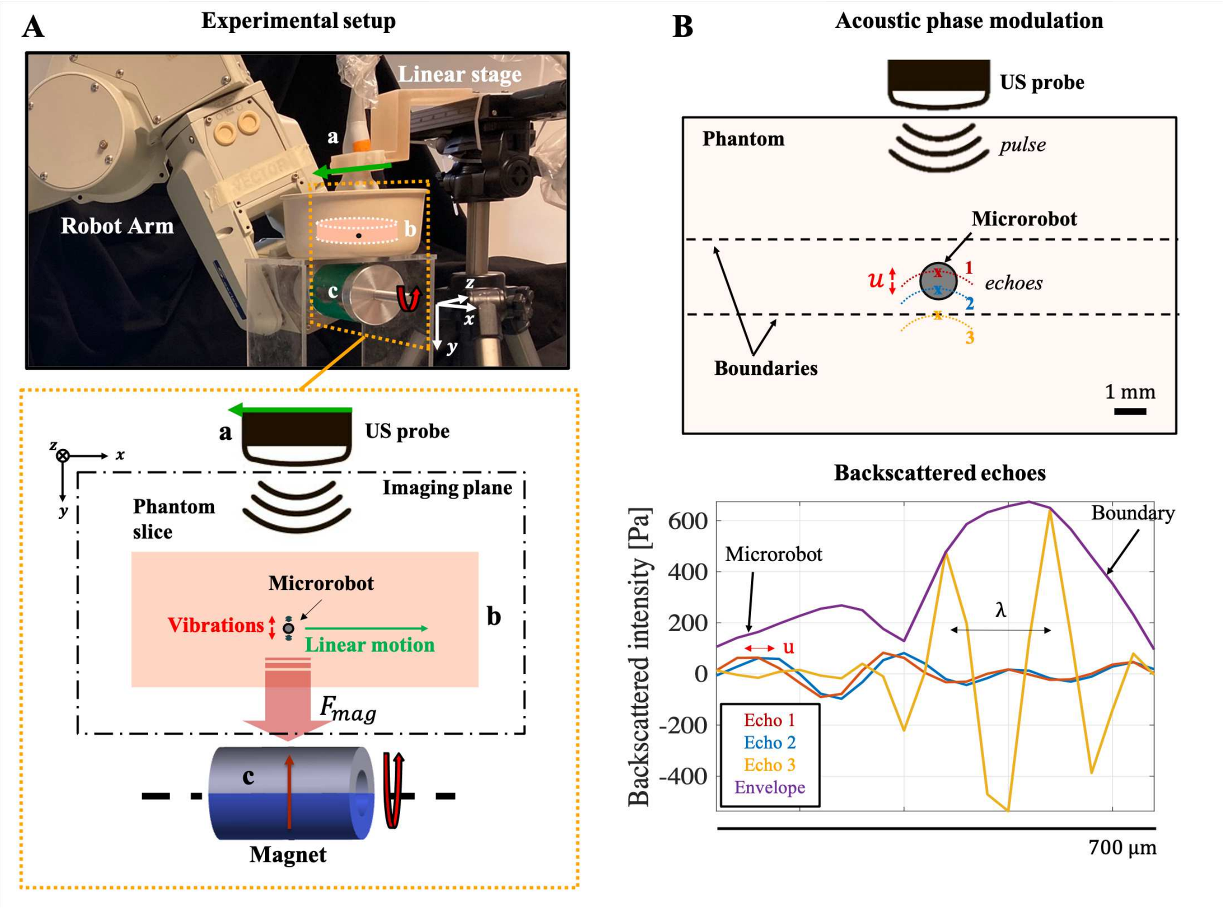
A
Experimental setup
Linear stage
a
Robot Arm
b
c
z
x
y
a
US probe
z
x
y
Imaging plane
Phantom
slice
Microrobot
Vibrations
Linear motion
b
F_{mag}
c
Magnet
B
Acoustic phase modulation
US probe
Phantom
pulse
Microrobot
u
1
2
3
echoes
Boundaries
1 mm
Backscattered echoes
Backscattered intensity [Pa]
600
400
200
0
-200
-400
Boundary
Microrobot
λ
u
Echo 1
Echo 2
Echo 3
Envelope
700 µm

Applied Physics Letters
ACCEPTED MANUSCRIPT
This is the author's peer reviewed, accepted manuscript. However, the online version of record will be different from this version once it has been copyedited and typeset.
PLEASE CITE THIS ARTICLE AS DOI: 10.1063/5.0032969

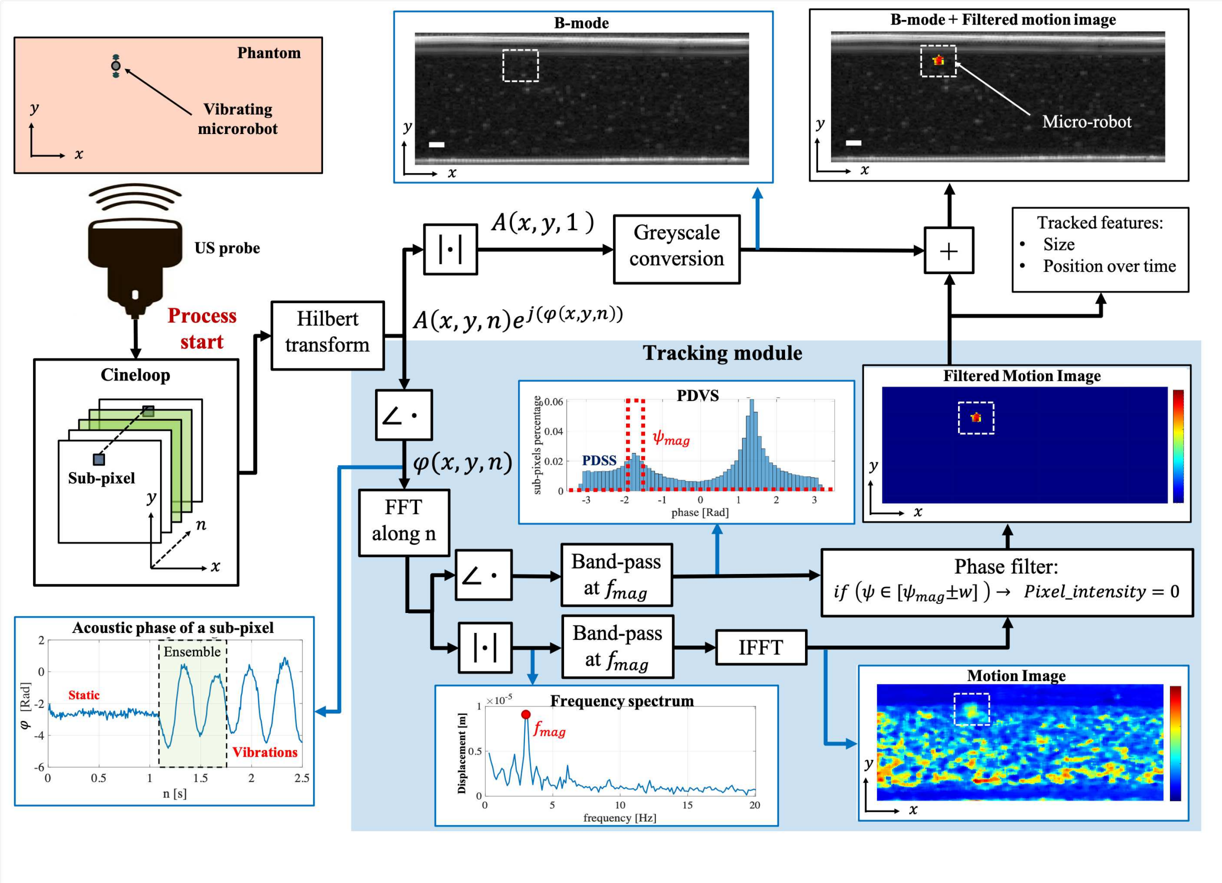
Phantom
Vibrating microrobot
y
x
US probe
Process start
Cineloop
Sub-pixel
y
n
x
Hilbert transform
B-mode
B-mode + Filtered motion image
Micro-robot
|·|
$A(x,y,1)$
Greyscale conversion
+
Tracked features:
- Size
- Position over time
$A(x,y,n)e^{j(\varphi(x,y,n))}$
Tracking module
∠·
$\varphi(x,y,n)$
FFT along n
PDVS
PDSS
ψ_{mag}
sub-pixels percentage
phase [Rad]
Filtered Motion Image
∠·
Band-pass at f_{mag}
Phase filter:
$if\ (\psi \in [\psi_{mag} \pm w]) \rightarrow\ Pixel\_intensity = 0$
|·|
Band-pass at f_{mag}
IFFT
Acoustic phase of a sub-pixel
Ensemble
Static
Vibrations
φ [Rad]
n [s]
Frequency spectrum
$\times 10^{-5}$
f_{mag}
Displacement [m]
frequency [Hz]
Motion Image

AIP Publishing

Applied Physics Letters
ACCEPTED MANUSCRIPT
This is the author's peer reviewed, accepted manuscript. However, the online version of record will be different from this version once it has been copyedited and typeset.
PLEASE CITE THIS ARTICLE AS DOI: 10.1063/5.0032969
AIP Publishing

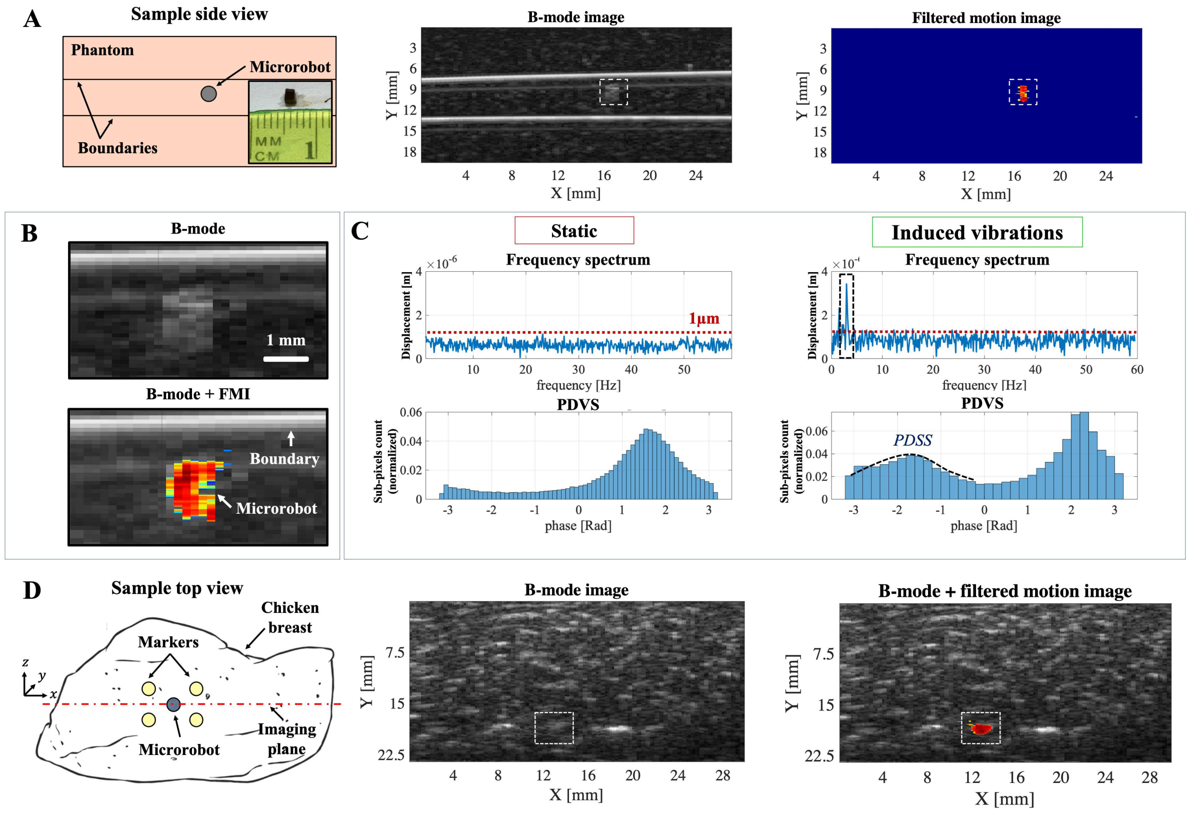
A
Sample side view
Phantom
Microrobot
Boundaries
MM
CM
1
B-mode image
Y [mm]
3
6
9
12
15
18
4
8
12
16
20
24
X [mm]
Filtered motion image
B
B-mode
1 mm
B-mode + FMI
Boundary
Microrobot
C
Static
Induced vibrations
Frequency spectrum
Displacement [m]
×10⁻⁶
1µm
frequency [Hz]
PDVS
Sub-pixels count (normalized)
phase [Rad]
PDSS
D
Sample top view
Chicken breast
Markers
Microrobot
Imaging plane
z
y
x
B-mode image
B-mode + filtered motion image
7.5
15
22.5
28

Applied Physics Letters ACCEPTED MANUSCRIPT

This is the author's peer reviewed, accepted manuscript. However, the online version of record will be different from this version once it has been copyedited and typeset.

PLEASE CITE THIS ARTICLE AS DOI: 10.1063/5.0032969

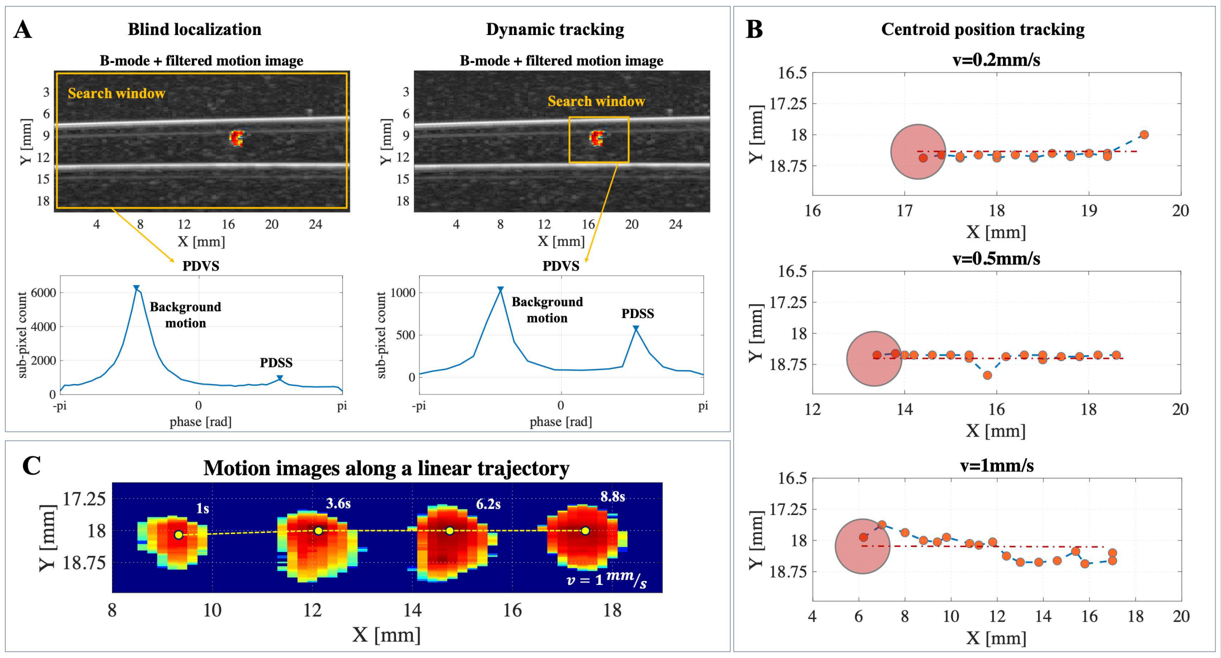AIP Publishing